Phase-Field Modeling of Domain Structure Energetics and Evolution in Ferroelectric Thin Films

Antonios Kontsos[1]

Chad M. Landis[2]
e-mail: landis@mail.utexas.edu

Department of Aerospace Engineering and Engineering Mechanics,
University of Texas at Austin,
Austin TX 78712-0235

A computational model developed based on the phase-field approach is used to model domain structures in ferroelectric thin films and to quantify the effects of strain and applied electric field on the microstructural evolution, and on the induced dielectric, electrostrictive, and piezoelectric film properties. Theoretically predicted vortex-like polydomain and experimentally observed bidomain and monodomain film morphologies are modeled using the continuum phase-field approach. A nonlinear finite element method is used to solve the boundary value problems relevant to ferroelectric thin films. The computed results agree with the Kittel law for specific ranges of film strain. Simulations that track the domain structure evolution and compute ferroelectric thin film properties given the film dimensions and the imposed electromechanical boundary conditions are also reported. [DOI: 10.1115/1.4000925]

Keywords: ferroelectrics, thin films, phase-field modeling, finite element methods, vortex domain structure

1 Introduction

A phase-field model previously developed by the authors [1,2] is used to investigate energetically favorable domain structures and their evolution in ferroelectric thin films subject to strain and applied electric field. The results demonstrate the role of film thickness and external loads on the domain structure, its evolution, and the nonlinear film properties. Fundamental ferroelectric constitutive behavior, domain morphology, and interactions with defects in ceramics and single crystals have been extensively studied over the past decades [3–5]. However, current device miniaturization processes and developments in microelectronics/nanoelectronics have raised the issue of length-scale dependent domain structures and constitutive behavior of ferroelectric thin films [6]. Research in this area is not new, as Landau [7] and Kittel [8] theoretically addressed the issue of the dependence of domain periodicity on film thickness for ferromagnets. Kittel [8] investigated a variety of energetically possible domain structures including monodomain, bidomain, and polydomain configurations and analyzed the film thickness values that favor various polarization distributions. Both Landau [7] and Kittel [8] suggested that in the absence of applied magnetic field, internal flux closure of magnetization could occur, and therefore highly ordered in-plane magnetization distributions are possible. Their theoretical predictions on ferromagnetic films were found by Mitsui and Furuichi [9] to be valid also for ferroelectrics. These authors investigated the domain structures in Rochelle Salt by using a polarization microscope and the domain width values they reported were found to be almost perfectly proportional to the square root of the crystal thickness. This relationship between domain size and film geometry constitutes the well-known Kittel law, which appears to hold for all ferroic materials [10].

Experimental observations of nanoscale 180 deg domains with polarization oriented perpendicular to the film surface (*c*-domains) in ferroelectric $PbTiO_3$ thin films were reported for the first time by Streifer et al. [11] using X-ray scattering. The film thickness in their experiments varied between 1.6 and 42 nm and the films were subject to epitaxial strain. They found that the Kittel law is valid even at this length scale. Similar domain structures and the validity of the Kittel law in $PbTiO_3$ thin films were also reported by Takahashi et al. [12] and Thompson et al. [13]. Schilling et al. [14] used scanning transmission microscopy to observe the structure of thin lamellae single crystal $BaTiO_3$ with thickness between 70 and 530 nm. They observed periodic arrays of 90 deg domains with widths varying according to the Kittel law.

To theoretically and computationally investigate domain structures that are energetically favorable in ferroelectric thin films, and to understand thin film constitutive behavior and its differences from bulk ferroelectrics, a variety of approaches have been proposed in the literature ranging from atomistic to continuum methods. Research using atomistic simulations has focused on predicting possible domain structures as a function of film dimensions and imposed mechanical and electrical boundary conditions. Fu and Bellaiche [15] presented a first-principles approach to investigate whether ferroelectricity can be suppressed in $BaTiO_3$ nanoparticles or not, and they concluded that there is no such critical dimension. In addition, they found that vortex-like polarization arrangements similar to the ones reported by Landau and Kittel are possible. Wu et al. [16] also used a first-principles approach to study the ferroelectric properties of lead zirconate titanate (PZT) films subject to different values of compressive strain. They computed domain structures with domain periodicity that changes according to the Kittel law as the film thickness increases. Additionally, Wu et al. [16] provided evidence of the effect of applied strain on the type of domain configurations observed in thin PZT films. They report that due to the clamping effect caused by the substrate, the strains imposed on the film affect its domain morphology, which for a thickness value of a few lattice parameters consists of alternating *c*-domains. Similar atomistic simulations of such domains in epitaxial PZT and barium titanate thin films subject to substrate constraint were per-

[1]Present address: Drexel University, 3141 Chestnut Street, Philadelphia, PA 19104.

[2]Corresponding author.

Contributed by the Applied Mechanics Division of ASME for publication in the JOURNAL OF APPLIED MECHANICS. Manuscript received July 8, 2009; final manuscript received October 8, 2009; published online April 16, 2010. Editor: Robert M. McMeeking.

formed by Lai and co-workers [17–19], who further investigated the effect of applied electric field on the evolution of the computed domain configurations. Their results demonstrate that the applied field strongly affects the type of possible domain patterns in ferroelectric thin films, which include monodomain, periodic stripe domain, and polydomain structures. Lai and co-workers [17–19] also showed the validity of the Kittel law for ferroelectric films by computationally observing changes in domain periodicity of vortex-like domain structures as a function of the film thickness.

Continuum approaches have also been proposed to model the domain structures in ferroelectric thin films. The majority of these methods rely on some form of a Landau-type thermodynamic potential. Catalan et al. [10] presented a phase-field analysis applied to ferroic materials, which is used to determine domain wall periodicity and the relationship between domain width and crystal thickness. Their approach theoretically reproduces the Kittel law. There have also been several computational phase-field modeling approaches to study ferroelectric thin film behavior. In phase-field models, the material polarization is usually chosen as the order parameter [20] and its spatial distribution defines domains and diffuse domain walls [21]. Li et al. [22] investigated the time evolution of the domain structure in ferroelectric films constrained by a rigid substrate. Their model provides various thermodynamically possible domain configurations as a function the compressive strain imposed by a substrate and temperature change. Schrade et al. [23] used a phase-field model that they implemented numerically using a finite element method. They reported a variety of domain structures including vortex-like polarization distributions based on given mechanical and electric boundary conditions. Dayal and Bhattacharta [24] studied the energetics of closure domain formation along with the effects of mechanical constraint on thin films.

Energetically favorable domain structures, dependence of their periodicity on film dimensions and mechanical strain, domain structure evolution under applied electric field, and the nonlinear dielectric, electrostrictive, and piezoelectric properties of thin films are investigated in this article using a phase-field model implemented within the finite element method. Vortex-like polydomain, bidomain, and monodomain structures are modeled for various levels of film strain and applied electric field. The results verify the Kittel law and the ferroelectric thin films properties are quantified as a function of the film strain.

2 Phase-Field Model

The phase-field approach used in this article has been developed previously by the authors, and has been applied to investigate interactions between ferroelectric domain walls and charged defects [1], as well as similar interactions with dislocations [2], and domain switching near crack tips [25]. We review here the governing electrical, mechanical and phase-field equations for completeness. Conservation of linear and angular momentum and the balances of stress in the volume and traction on a surface yield

$$\sigma_{ji,j} + b_i = 0 \quad \text{in } V \tag{1}$$

$$\sigma_{ij} = \sigma_{ji} \quad \text{in } V \tag{2}$$

$$\sigma_{ji} n_j = t_i \quad \text{on } S \tag{3}$$

where σ_{ij} are the components of the Cauchy stress tensor, b_i are the body forces per unit volume, n_i are the components of the unit vector normal to the surface, and t_i are the tractions applied to the surface. Summation over repeated indices is assumed and subscripts following commas represent partial differentiation with respect to the coordinate directions. Assuming linear kinematics, the following strain-displacement equations hold

$$\varepsilon_{ij} = \tfrac{1}{2}(u_{i,j} + u_{j,i}) \quad \text{in } V \tag{4}$$

where u_i are displacements and ε_{ij} are the small-strain tensor components. The electrostatic field equations are given as

$$E_i = -\varphi_{,i} \quad \text{in } V \tag{5}$$

$$D_{i,i} - q = 0 \quad \text{in } V \tag{6}$$

$$D_i n_i = -\omega \quad \text{on } S \tag{7}$$

where E_i is the electric field, φ is the electric potential, q is the volume charge density, ω is the surface charge density, and D_i are the components of the electric displacement defined as

$$D_i = \kappa_0 E_i + P_i \tag{8}$$

In Eq. (8) κ_0 is the permittivity of free space and P_i are the components of material polarization, which is the order parameter for the phase-field model. This choice of order parameter leads to a functional dependence of the material free energy on the polarization and its gradients. To account for this dependence a work-conjugate microforce approach has been proposed [1,26], which yields the following governing equations:

$$\xi_{ji,j} + \pi_i + \gamma_i = 0 \quad \text{in } V \tag{9}$$

$$\sigma_{ji} = \frac{\partial \psi}{\partial \varepsilon_{ij}}, \quad E_i = \frac{\partial \psi}{\partial D_i}, \quad \xi_{ji} = \frac{\partial \psi}{\partial P_{i,j}}, \quad \eta_i \equiv \frac{\partial \psi}{\partial P_i} \tag{10}$$

$$\pi_i = -\eta_i - \beta_{ij}\dot{P}_j \tag{11}$$

where ξ_{ij} is a material microforce tensor, π_i is an internal microforce vector, γ_i is an external microforce vector, η_i is simply defined to be the partial derivative of the free energy with respect to the polarization components, and β_{ij} is the polarization viscosity tensor, which must be positive definite. The generic form of the Helmholtz free energy is given in Eq. (12). This form is able to fit the spontaneous polarization and strain as well as the linear piezoelectric, dielectric, and elastic properties of barium titanate about the stress-free spontaneous polarization and strain states

$$\begin{aligned}\psi = {} & \frac{1}{2} a_{ijkl} P_{i,j} P_{k,l} + \frac{1}{2} \bar{a}_{ij} P_i P_j + \frac{1}{4} \bar{\bar{a}}_{ijkl} P_i P_j P_k P_l \\ & + \frac{1}{6} \bar{\bar{\bar{a}}}_{ijklmn} P_i P_j P_k P_l P_m P_n + \frac{1}{8} \bar{\bar{\bar{\bar{a}}}}_{ijklmnrs} P_i P_j P_k P_l P_m P_n P_r P_s \\ & + b_{ijkl} \varepsilon_{ij} P_k P_l + \frac{1}{2} c_{ijkl} \varepsilon_{ij} \varepsilon_{kl} + \frac{1}{2} f_{ijklmn} \varepsilon_{ij} \varepsilon_{kl} P_m P_n \\ & + \frac{1}{2} g_{ijklmn} \varepsilon_{ij} P_k P_l P_m P_n + \frac{1}{2\kappa_0} (D_i - P_i)(D_i - P_i)\end{aligned} \tag{12}$$

Details about a specific form of the free energy and values for its coefficients are included in the Appendix and the references therein.

3 Finite Element Implementation

Solutions to Eqs. (1)–(12) can be obtained numerically using the finite element method. The nodal degrees of freedom are chosen to include the mechanical displacements, the polarization components, and the electric potential, from which strains, polarization gradients, and electric field values are computed within the elements. The following statement of the principal of virtual work is used to implement the finite element method

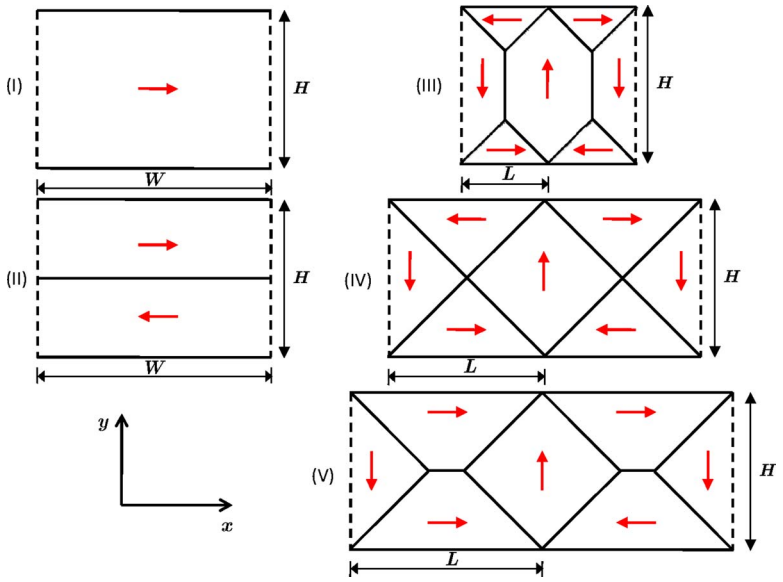

Fig. 1 The types of domain structures in ferroelectric thin films modeled in this article. The arrows designate the direction of polarization vectors. Type (I) corresponds to monodomains in the *x*-direction, type (II) to bidomains, and types (III)–(V) to different vortex structures. The height of the film is *H*, and its width is equal to 2*L*, which corresponds to the domain periodicity in types (III)–(IV). The solids lines inside these models indicate 180 deg and 90 deg domain walls. Periodic boundary conditions are imposed on the broken lines on the side and various electromechanical conditions are chosen for the top and bottom boundaries.

$$\int_V \beta_{ij}\dot{P}_j\delta P_i dV + \int_V (\sigma_{ji}\delta\varepsilon_{ij} - D_i\delta E_i + \eta_i\delta P_i + \xi_{ji}\delta P_{i,j})dV$$
$$= \int_S (b_i\delta u_i - q\delta\varphi + \gamma_i\delta P_i)dV + \int_S (t_i\delta u_i - \omega_i\delta\varphi + \xi_{ji}n_j\delta P_i)dS \tag{13}$$

Standard finite element procedures lead to a set of nonlinear algebraic equations for the nodal degrees of freedom, and the solution is obtained using an iterative Newton–Raphson method. Details on the numerical implementation of the phase-field model can be found in Ref. [1]. All of the results reported in this work are for equilibrium domain structures. As such, the first integral in Eq. (13) including the polarization rates is always zero; however, in some cases this term is implemented to allow a domain structure to evolve along a nonequilibrium path towards its final stable state.

The domain structures investigated in this article are presented in Fig. 1. The top and bottom solid lines of these models designate microforce free surfaces. In Sec. 4 various boundary conditions are imposed to account for the strain exerted on the films by the substrate and the externally applied electric field. The periodic boundary conditions listed in Eq. (14) are imposed on the vertical broken lines; $2L$ is the wavelength of the domain structure periodicity

$$u_x(-L,y) = u_x(L,y) + 2L\frac{\partial u_x}{\partial x}$$
$$u_y(-L,y) = u_y(L,y)$$
$$\varphi(-L,y) = \varphi(L,y) \tag{14}$$
$$P_x(-L,y) = P_x(L,y)$$
$$P_y(-L,y) = P_y(L,y)$$

In Fig. 1, type (I) corresponds to a monodomain, which constitutes the energetic ground state for the tetragonal phase of spontaneously polarized ferroelectric material when no electric field or stress is applied. This ground state is used in Sec. 4 to normalize total energy values computed for various domain configurations. Note that the monodomain state is not necessarily the minimum energy configuration when the film is stressed. Type (II) corresponds to a bidomain structure with polarization vectors aligned parallel to the film surface. Types (III), (IV), and (V) correspond to vortex-like polydomain polarization distributions that, as mentioned in Sec. 1, have been theoretically predicted to occur in ferromagnetic thin films and have been also found by first-principles calculations to be energetically favorable under appropriate electromechanical boundary conditions in ferroelectrics. We will show that type (III) is most favorable when the surfaces of the film are insulated and the film strain is compressive, while type (V) is favored when the surfaces are electroded and the film strain is tensile. The rotation of the polarization vector near the surfaces creates 90 deg domain walls (closure domains) in addition to the 180 deg walls further away from the surfaces. Note that domain walls in phase-field models are diffuse and their width defines a characteristic material length scale l_0

$$l_0 = \sqrt{\frac{a_0 P_0}{E_0}} \tag{15}$$

where a_0 is a coefficient of the exchange energy term in the free energy form given in Eq. (12) (see the Appendix), P_0 is the spontaneous polarization, and E_0 is the characteristic electrical field value required to cause homogeneous 180 deg switching in a spontaneously polarized monodomain. Values for these parameters for barium titanate can be found in the Appendix. The minimum energy states for these polarization distributions for given values of film thickness and in-plane strain are computed in Sec. 4 by varying the domain periodicity wavelength. The results demonstrate the effect of film strain on the domain structure and vali-

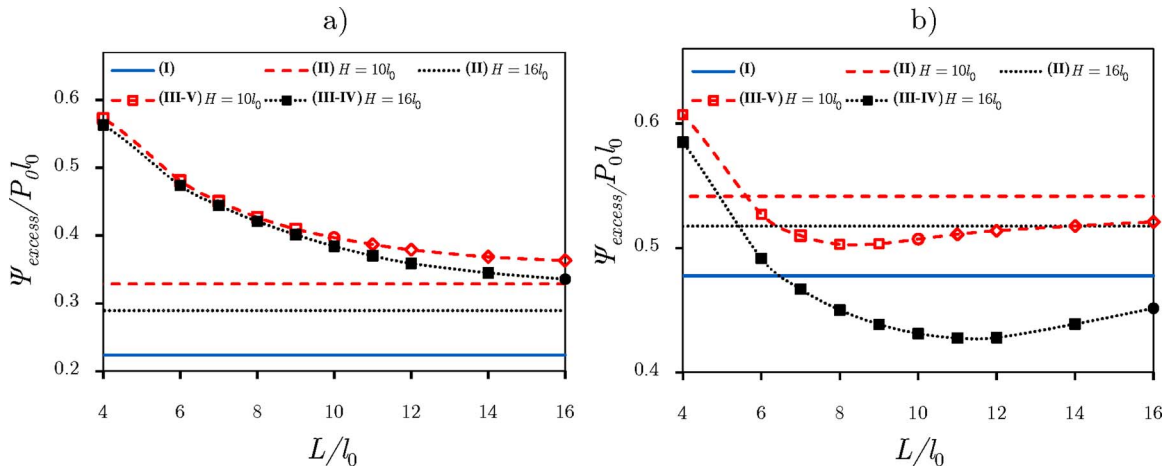

Fig. 2 (*a*) **Excess energy values computed for the monodomain (I), the bidomain (II), and the vortex structures (III–V) of Fig. 1 as a function of the domain periodicity, for two values of film thickness equal to $10l_0$ and $16l_0$ and film strain $\varepsilon_{xx}=0.3\varepsilon_0$. (*b*) Similar results for film strain $\varepsilon_{xx}=0.07\varepsilon_0$.**

date the Kittel law. In addition, the effect of applied electric field on the evolution of the domain structure and on the properties of ferroelectric thin films is simulated in Sec. 4.

4 Insulated Films

One of the theoretically predicted and experimentally verified characteristics of ferroelectric thin film behavior is the Kittel law, which, as outlined in Sec. 1, applies to all ferroic materials and spans a wide range of length scales. According to this law, in ferroelectric thin film structures consisting of periodic domain patterns the domain width values that are energetically most favorable to occur are proportional to the square root of the film thickness. The Kittel law applies to domain structures with morphologies similar to type (III) with the long axis of the domains perpendicular to the film surface. For such structures the Kittel law arises by minimizing the combination of the field energy (elastic, electrical, and magnetic), which is proportional to the wavelength of the domain periodicity L per film area, and the domain wall energy, which is proportional to the film thickness H and inversely proportional to L. This minimization procedure produces the relationship $L \propto \sqrt{H}$ between the minimum energy domain periodicity and the film thickness.

For the models shown in Fig. 1 and to investigate the validity of the Kittel law in ferroelectric thin films, the top surface of the film is assumed to be traction and charge free and the bottom surface is assumed to be charge free but bonded to a rigid substrate. In addition to the periodic boundary conditions listed in Eq. (14), the following boundary conditions are imposed on the top and bottom surfaces

$$t_x(x,H/2)=0, \quad -L \le x \le L \tag{16}$$

$$t_y(x,H/2)=0, \quad -L \le x \le L \tag{17}$$

$$u_x(x,-H/2)=\varepsilon_{xx}x, \quad -L \le x \le L \tag{18}$$

$$u_y(x,-H/2)=0, \quad -L \le x \le L \tag{19}$$

$$\omega(x,\pm H/2)=0, \quad -L \le x \le L \tag{20}$$

Note that the origin is assumed to be at the centroid of each model. The in-plane strain ε_{xx} is imposed on the film through its attachment to a substrate material. This in-plane strain can be caused by the lattice mismatch between the substrate material and the film, or perhaps by thermal expansion mismatch. To determine the effect of the strain on the morphology of ferroelectric thin films and their properties, different values of strain are imposed according to Eq. (18). In this work, the reference strain corresponds to the cubic state of the material. All strain values are normalized by the spontaneous strain ε_0. For an in-plane strain level of $\varepsilon_{xx}=\varepsilon_0$, a monodomain polarized parallel to the film surface (*a*-domain), as shown in Fig. 1 type (I), can reside in the stress and electric field free minimum energy state. For an in-plane strain of $\varepsilon_{xx}=-0.32\varepsilon_0$ (for $BaTiO_3$), a monodomain polarized perpendicular to an electroded film surface (*c*-domain) can reside in a stress and electric field free minimum energy state. These two domain states/orientations are sometimes referred to *a*- and *c*-domains, respectively, i.e., either the *a* or *c* lattice direction is perpendicular to the film surface.

Figures 2(*a*) and 2(*b*) present excess energy values per unit area computed using equilibrium solutions of the thin film structures shown in Fig. 1, with varying domain periodicity, film thickness, and film strain. In Figs. 2(*a*) and 2(*b*) the excess film energy is defined as

$$\psi_{\text{excess}} = \frac{1}{2LH}\int_{-H/2}^{H/2}\int_{-L}^{L}\psi dxdy - \psi_0 \tag{21}$$

where the integral represents the numerically computed free energy for a given equilibrium solution, and ψ_0 is the absolute minimum of the Helmholtz free energy. In Fig. 2(*a*) results are given for two different thickness values and include the monodomain (solid line) or type (I), the bidomain (dotted lines) or type (II), and the vortex domain structures (markers) or types (III–V). Figure 2(*a*) shows that for a film strain of $\varepsilon_{xx}=0.3\varepsilon_0$, no minimum energy exists for the vortex states, and the energy of these states is bounded from below by the bidomain energy for a given film thickness H. Additional calculations confirm that similar behavior exists for all strain levels $\varepsilon_{xx}>0.3\varepsilon_0$. For the bidomain and vortex polarization distributions, an increase in film thickness causes a decrease in the excess film energy, while such a thickness change has no effect on the monodomain energy. Furthermore, symmetry dictates that the size of the periodic cell has no effect on the monodomain and bidomain energies, whereas the vortex energies are affected by the value of domain periodicity, as shown in Fig. 2(*a*).

Results similar to the ones presented in Fig. 2(*a*) are plotted in Fig. 2(*b*) for a smaller value of film strain than that in Fig. 2(*a*). For this strain level, the monodomain and bidomain energies shift higher with respect to the corresponding energies in Fig. 2(*a*). This effect occurs due to the compressive stresses imposed upon the film by the rigid substrate. Recall that for the *a*-domain orientation the stresses vanish at a film strain of $\varepsilon_{xx}=\varepsilon_0$, and strain

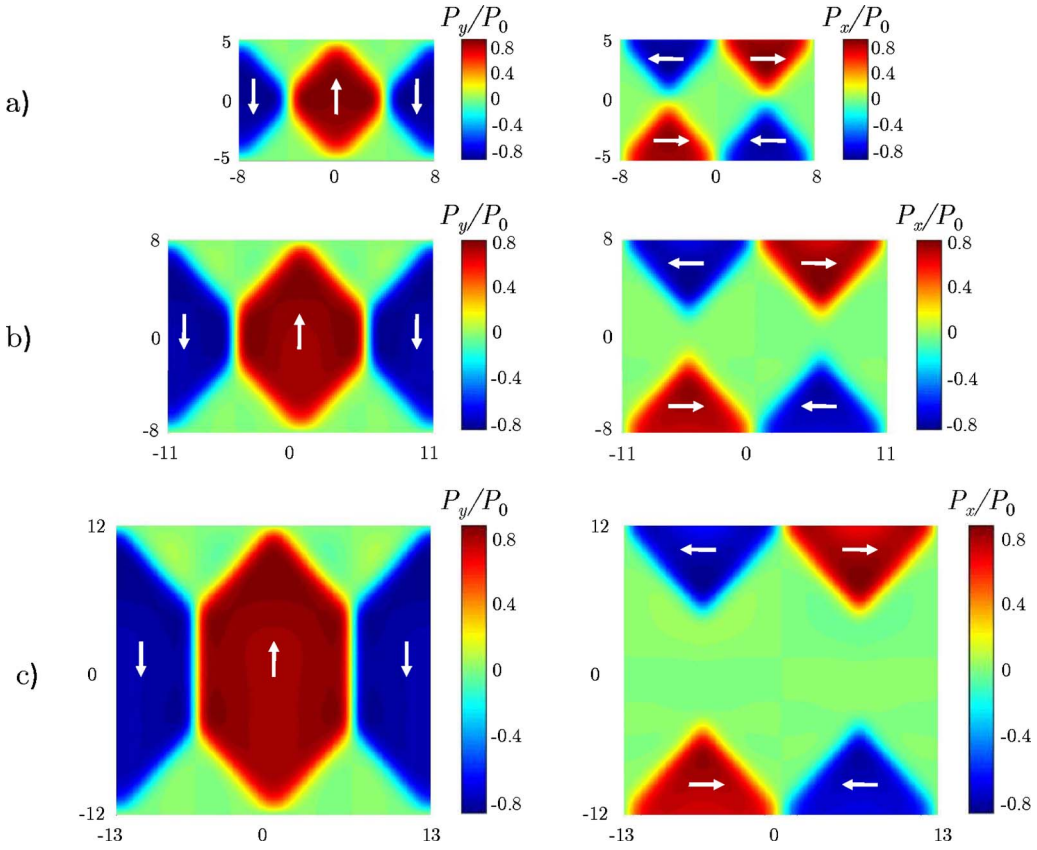

Fig. 3 Minimum energy equilibrium polarization distributions in the *x*- and *y*-directions computed for film strain $\varepsilon_{xx}=0.07\varepsilon_0$. The contour plots are consistent with the data presented in Fig. 2(*b*). The solid white arrows designate the direction of polarization vectors and have magnitudes normalized by the spontaneous value P_0. Three thickness values are used and are equal to (*a*) $10l_0$, (*b*) $16l_0$, and (*c*) $24l_0$.

levels smaller than this induce compressive stresses. In addition, the dependence of the energy on the domain periodicity for the vortex structures changes qualitatively in Fig. 2(*b*) with the emergence of a minimum. This behavior appears for strain levels $\varepsilon_{xx} < 0.3\varepsilon_0$. Note that this specific value of $0.3\varepsilon_0$ is certainly not universal, but rather valid for the model implemented here for $BaTiO_3$. For the film strain $\varepsilon_{xx}=0.07\varepsilon_0$ and for both values of film thickness used, distinct minima that correspond to different domain periodicities are computed. The results in Fig. 2(*b*) indicate that the increase in film thickness is associated with an increase in the minimum energy domain periodicity computed for $\varepsilon_{xx}=0.07\varepsilon_0$. Note that the minima in Fig. 2(*b*) correspond to type (III) vortex structures for both values of the film thickness presented. Additional results for other film thickness values have shown that the corresponding minimum energy domain periodicity is always a type (III) domain structure. In Fig. 2(*b*) different markers have been used to designate the type of vortex structure for each value of domain periodicity and show that although the vortex structure may change as the domain periodicity increases, the variation observed in the computed energies is smooth at the crossover from type (III) to type (V). Furthermore, for film thicknesses $H>12l_0$ the minimum energy for type (III) vortices is actually less than the monodomain energy. Hence, for the vortex structure the additional domain wall energy is offset by the reduction in the strain energy associated with the additional *c*-domains.

The computational model was used to investigate the equilibrium domain structures for a range of film strain, film thickness, and domain periodicity values. Figures 3(*a*)–3(*c*) present results for the polarization distributions associated with the findings in Fig. 2(*b*) for three different values of film thickness. In the contour plots of Figs. 3(*a*)–3(*c*) the domain width values *L*, which correspond to minimum energy equilibrium solutions increase as the film thickness increases. As will be shown in Fig. 4, this relationship is in accordance with the Kittel law. Note that the domain structures presented in Figs. 3(*a*)–3(*c*) correspond to type (III) shown in Fig. 1. With regard to the Kittel law, the existence of the closure domains near the film surfaces implies that the bulk energy, which favors a finer domain structure, is not driven solely by electrostatics as in the analysis of stripe domains by Mitsui and Furuichi [9], but rather by the electro-elastic energy required to

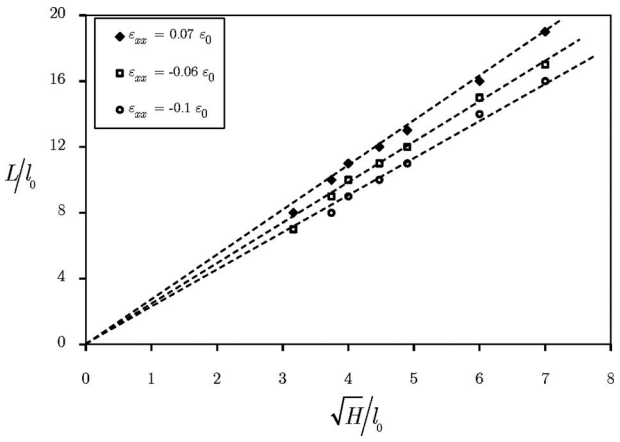

Fig. 4 Domain width values that correspond to minimum energy equilibrium solutions for the polarization distributions in ferroelectric thin films are plotted as a function of the square root of film thickness for three different values of film strain. The computed results agree with the Kittel law.

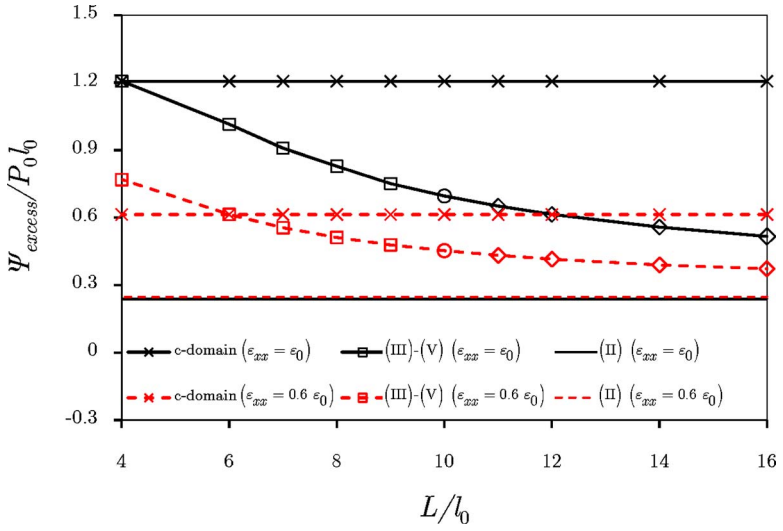

Fig. 5 Excess energy values computed for monodomain structures with polarization vectors in the direction of the applied electric field (i.e., *c*-domains), bidomain structures with polarization vectors aligned in a direction parallel to the film surface and therefore similar to type (II) of Fig. 1 and polydomain structures for different values of domain periodicity, film thickness equal to $10l_0$ and two levels of film strain $\varepsilon_{xx}=\varepsilon_0$ and $\varepsilon_{xx}=0.6\varepsilon_0$.

"mend" the strain incompatibilities between the *a*- and *c*-type domains, see, for example, Ref. [24] for a more detailed discussion.

In Fig. 4, the minimum energy domain width values for three different film strains are plotted as a function of the square root of the film thickness. These results agree with the proportionality relationship dictated by the Kittel law. In addition, Fig. 4 demonstrates the role of film strain on one aspect of the domain morphology in ferroelectric thin films. Specifically, as the film strain decreases, smaller domain widths are energetically favored.

5 Electroded Films

The calculations presented and described in Figs. 2(*a*) and 4 are for thin films assuming that both the top and bottom surfaces are perfectly insulated electrically. Of greater technological interest is the case where the top and bottom surfaces are contacted with electrodes and a voltage is applied across the film. To investigate the effect of applied electric field on the domain structure and its evolution in ferroelectric thin films, and to quantify the dielectric, piezoelectric, and electrostrictive properties, the following electric boundary conditions are applied on the top and bottom surfaces of the models presented in Fig. 1, in addition to the mechanical conditions given in Eqs. (16)–(19)

$$\varphi(x,-H/2)=0, \quad -L\le x\le L \tag{22}$$

$$\varphi(x,H/2)=-EH, \quad -L\le x\le L \tag{23}$$

where E is the averaged applied electric field in the y-direction and H is the film thickness.

The first set of simulations has been performed in order to determine if the electroded films have minimum energy structures similar to those found for the insulated films. Figure 5 presents the excess energy values similar to those shown in Figs. 2(*a*) and 2(*b*), for a given film thickness, two different film strain values, and applied electric field equal to zero. The domain structures investigated in Fig. 5 include homogeneous *c*-domains with the polarization aligned in a direction perpendicular to the film surface (i.e., not type (I)), type (II) bidomains, as shown in Fig. 1, and vortex (types III–V) structures similar to the ones presented in Fig. 1. The results in Fig. 5 indicate that electroded ferroelectric thin films do not have a minimum energy domain periodicity as computed for the insulated films, and that the energy of the vortex structure is bounded from below by the bidomain structure. Furthermore, for the strain states shown, a homogeneous *a*-domain (type (I)) is the minimum energy structure. Nevertheless, for a significant range of domain widths, the energy of the vortex domain structure is in fact lower than the *c*-domain state for large film strains. Hence, the vortex structures constitute metastable states with the potential for interesting domain structure evolution during the application of electric field. Additionally, larger film strains and larger domain widths tend to stabilize the vortex domain morphology over the *c*-domain state.

In order to generate the domain structures for the electroded films, the structures for the insulated films were used as initial conditions, and the field solutions were allowed to evolve to equilibrium using the dissipative polarization viscosity term in Eq. (13). Figures 6(*a*)–6(*c*) illustrate such an evolution of the film microstructure toward equilibrium for no applied electric field. The contour plots shown in this figure correspond to the results in Fig. 5 and demonstrate the effect of different electromechanical conditions on the equilibrium domain morphologies of ferroelectric thin films. The first set of plots in Figs. 6(*a*)–6(*c*) corresponds to an evolution step close to the initial conditions for the type (III) vortex. Due to the electroded top and bottom surfaces the microstructure evolves and new *c*-domains with polarization vectors in the y-direction are formed at the center and corners of the models shown in Figs. 6(*a*)–6(*c*), and the shape of the domains with polarization in the x-direction changes as well. The third set of plots in Figs. 6(*a*)–6(*c*) correspond to the computed equilibrium solution and shows that the newly formed *c*-domains grow even more forming a checkerboard pattern of elongated hexagonal domains. Note that there is a considerable difference in morphology between the insulated and electroded films for the same film thickness and strain.

The effect of the film thickness on the equilibrium domain structures in electroded ferroelectric thin films is displayed in Figs. 7(*a*)–7(*c*). Equilibrium polarization distributions are plotted in this figure for three different thickness values, given the domain periodicity and film strain. In contrast to the insulated films, the results demonstrate significant changes in the domain morphology of the films with varying thickness. The first set of plots corresponds to the equilibrium solutions presented in Figs. 6(*a*)–6(*c*) in which *c*-domains elongated in the x-direction develop. For slightly

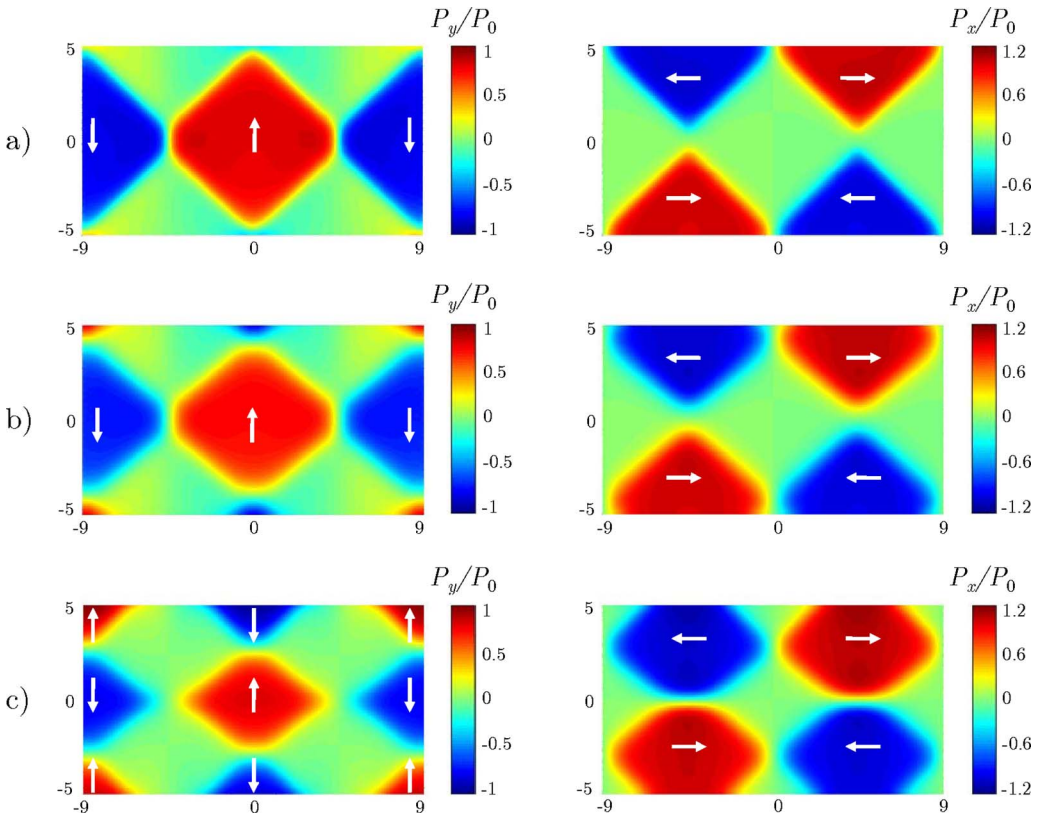

Fig. 6 Evolution of the polarization distributions in the *x*- and *y*-directions normalized by the spontaneous polarization for zero applied electric field. The domain periodicity is equal to $18l_0$, the film thickness equal to $10l_0$ and the film strain is equal to the spontaneous value. The first two sets of plots correspond to nonequilibrium evolution states and the third one is the equilibrium solution for applied field equal to zero.

larger thickness values, the central hexagonal domain is distorted and has increased its size as indicated in the second set of plots or has been duplicated and reduced its size as shown in the third set. The last set of plots actually suggests that new domains can form out of existing ones due to electro-elastic and domain wall interactions caused by the application of the electromechanical boundary conditions. Significant changes are also observed in the domains with polarization vectors in the *x*-direction.

In Figs. 8(*a*)–8(*c*) contour plots for thin film equilibrium polarization distributions in the *x*- and *y*-directions are presented for different values of the applied electric field. The domain periodicity, film thickness, and film strain values chosen to compute the equilibrium solutions shown in Figs. 8(*a*)–8(*c*) correspond to those used to compute the results for Figs. 6(*a*)–6(*c*). The first set of plots in Figs. 8(*a*)–8(*c*) shows polarization distributions for zero applied electric field. As the applied field increases from zero to some positive value, domains with polarization aligned with the field increase their size at the expense of domains with polarization opposite to the direction of the field, as shown by the second set of plots. Note that the domains with polarization vectors in the *x*-direction also change their shape significantly as the field increases. Similar observations are made for the third set of plots in Figs. 8(*a*)–8(*c*), which corresponds to the maximum value of external electric field that can be applied to the film prior to the film switching to a single *c*-domain. In this electrically loaded state the *c*-domain in the center, with polarization in the direction of the applied field, has significantly increased its size, while the *c*-domains with opposite polarization have decreased magnitudes and form a diamond-like band around the central domain. During this process the *a*-domains become narrower. Similar results have been computed for negative applied fields, in which case the evolution of the domain structure follows an analogous pattern with the critical field opposite to the maximum positive value used to plot the results in Figs. 8(*a*)–8(*c*). It is of interest to note that this critical field level is approximately twice that needed to homogeneously switch a stress-free *c*-domain, implying that the film strain has a significant stabilizing effect on the polydomain structure.

Figures 8(*a*)–8(*c*) represent one example of the domain structure evolution within a thin film during the application of electric field for a given film thickness, strain, and domain structure periodicity. Simulations with fixed film thickness $H=10l_0$, domain periodicity $2L=18l_0$, and strains in the range of $0.2\varepsilon_0 \leq \varepsilon_{xx} \leq 1.1\varepsilon_0$ were performed in order to investigate the role of the strain on the behavior of the film. The simulations reveal that strain controls transitions in the film behavior, similar to the way that temperature controls the phase transitions in bulk material. Figures 9(*a*)–9(*c*) illustrate three different domain structures corresponding to different strain-induced transitions in the film behavior. The corresponding plots of the dielectric response, spontaneous polarization, critical electric field, electrostrictive/piezoelectric strain, and stress in the film are shown in Figs. 10(*a*) and 10(*b*).

For strains $\varepsilon_{xx} > 0.54\varepsilon_0$ the net behavior of the film appears to be "paraelectric" with zero averaged polarization when no electric field is applied. Figure 9(*a*) illustrates the domain structure for this strain range. Note that Fig. 9(*a*) is the same domain structure as that in Fig. 8(*a*), but with the viewing area shifted by *L* in the *x*-direction. For these strain states the dielectric response is nonlinear but reversible up to a critical field level of E_c, beyond which the film switches to a homogeneous *c*-domain. Figure 10(*a*) plots

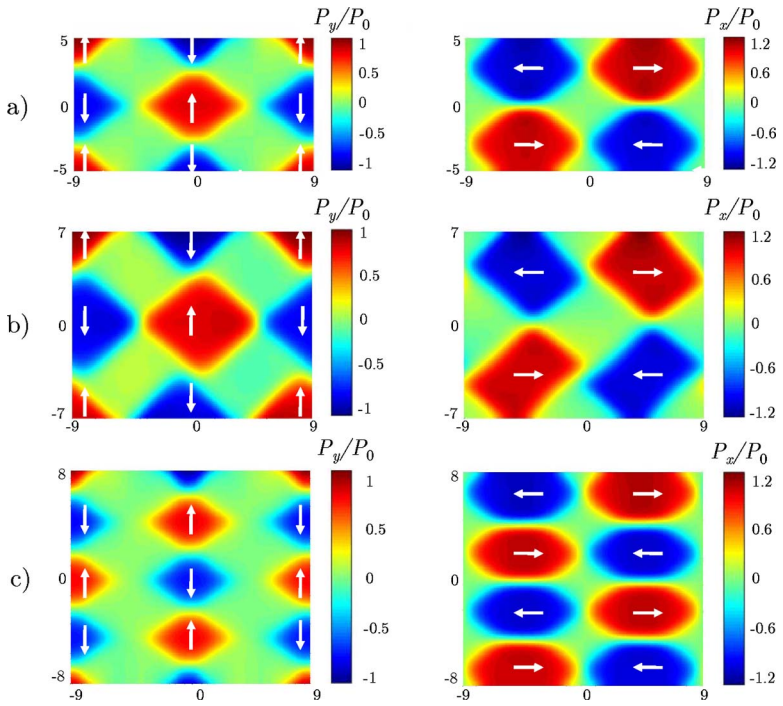

Fig. 7 Equilibrium polarization distributions in the *x*- and *y*-directions normalized by the spontaneous polarization for zero electric field, domain periodicity equal to $18l_0$ and film strain $\varepsilon_{xx}=\varepsilon_0$. Three different values of film thickness are used and are equal to (*a*) $10l_0$, (*b*) $14l_0$, and (*c*) $16l_0$.

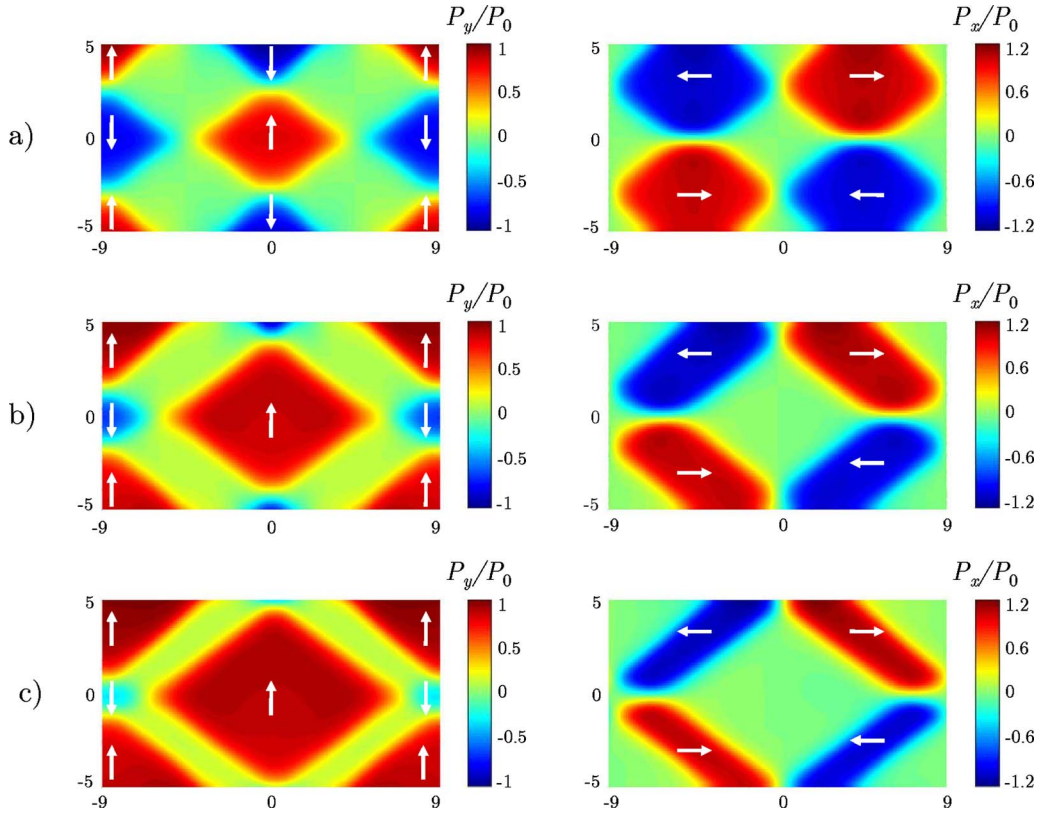

Fig. 8 Equilibrium polarization distributions in the *x*- and *y*-directions normalized by the spontaneous polarization for different values of applied electric field (*a*) $E=0$, (*b*) $E=1.0\ E_0$, and (*c*) $E=2.066\ E_0$. The domain periodicity is equal to $18l_0$, the film thickness equal to $10l_0$ and the film strain is $\varepsilon_{xx}=\varepsilon_0$.

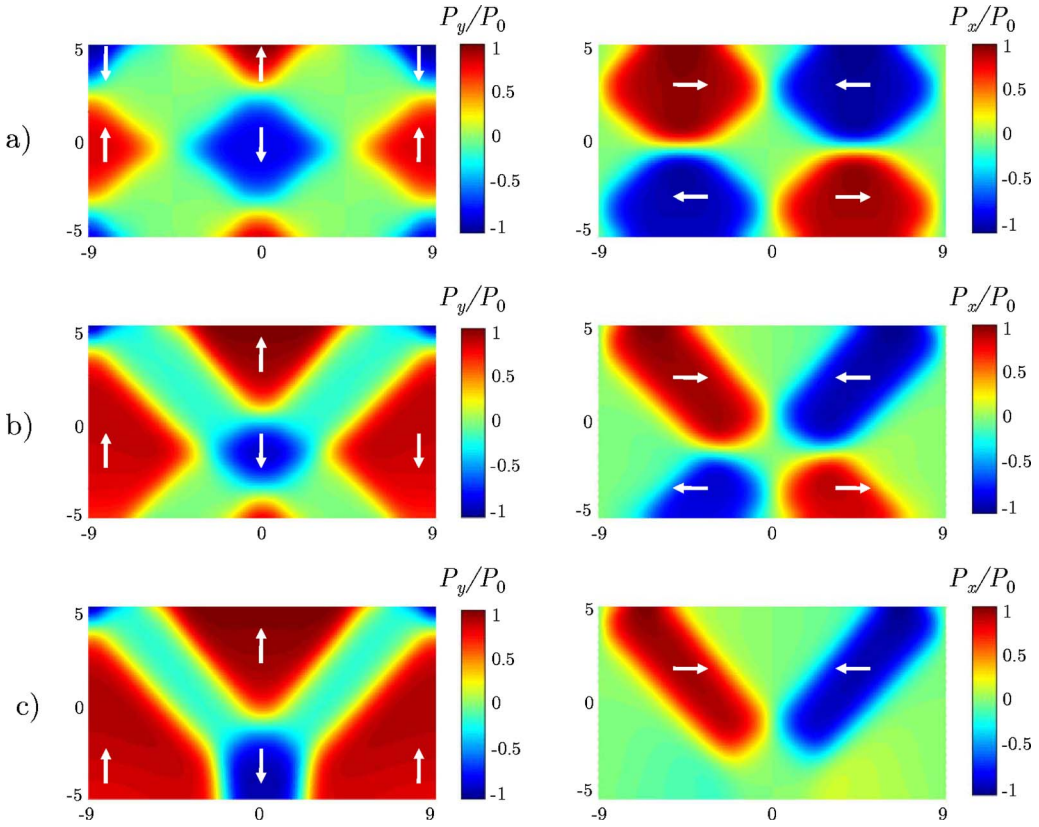

Fig. 9 Equilibrium polarization distributions in the *x*- and *y*-directions normalized by the spontaneous polarization for different values of film strain. The domain periodicity is equal to $18l_0$ and the film thickness is equal to $10l_0$. (*a*) $\varepsilon_{xx}=0.6\varepsilon_0$, (*b*) $\varepsilon_{xx}=0.4\varepsilon_0$, and (*c*) $\varepsilon_{xx}=0.3\varepsilon_0$.

the averaged electric displacement in the y-direction, i.e., the charge per area stored on the electrodes, as a function of the applied electric field. Figure 10(*b*) plots the effective spontaneous polarization of the film P_s, which is zero for $\varepsilon_{xx}>0.54\varepsilon_0$, and the critical electric field E_c as a function of the film strain ε_{xx}. The results demonstrate that tensile strains have a stabilizing effect on the film, with E_c growing as the film strain increases. Furthermore, it is notable that the domain structure shown in Fig. 9(*a*) can sustain average fields that are larger that the field required for stress-free, homogeneous, 180 deg switching. Figures 11(*a*) and 11(*b*) illustrate that the film behaves in an electrostrictive manner for $\varepsilon_{xx}>0.54\varepsilon_0$, with the actuating strain ε_{yy} and the film stress σ_{xx} varying as an even function of the applied electric field.

At the strain level $\varepsilon_{xx}=0.54\varepsilon_0$, the film behavior changes, in a manner akin to a second order continuous transition, where the overall film transforms from a paraelectric type of response to a "ferroelectric" response. Note that we referring to the macroscopic film response. Each material point in the film remains ferroelectric for all cases. This behavior is demonstrated clearly in Figs. 9(*a*)–9(*c*) and 11(*b*). Figure 10(*b*) shows that for film strain values $\varepsilon_{xx}<0.54\varepsilon_0$ the film has a nonzero net spontaneous polarization. Figure 9(*b*) illustrates that this occurs due to the positively

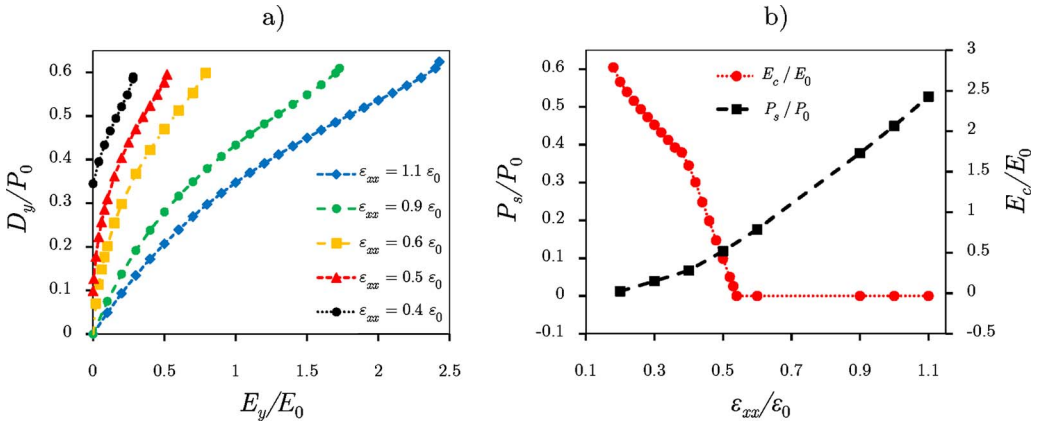

Fig. 10 (*a*) Electric displacement in the *y*-direction as a function of applied electric field in the same direction for several values of film strain and for a thin film with domain periodicity equal to $18l_0$ and thickness equal to $10l_0$. (*b*) Effective spontaneous polarization and critical electric field in the *y*-direction as a function of the film strain.

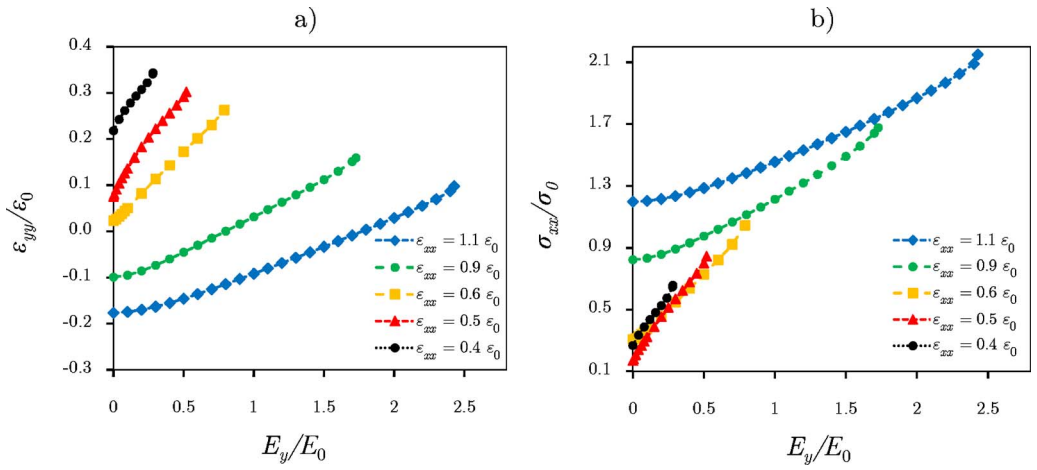

Fig. 11 (*a*) Normalized strain in the *y*-direction and (*b*) normalized stress in the *x*-direction as a function of applied field in a direction perpendicular to the film surface for several values of film strain, domain periodicity equal to $18l_0$ and thickness equal to $10l_0$

polarized central *c*-domains growing(shrinking) and the negatively polarized *c*-domains shrinking(growing) for a net positive(negative) film polarization. Figures 11(*a*) and 11(*b*) show the corresponding transition from electrostrictive to piezoelectric behavior with the actuating strain ε_{yy} and film stress σ_{xx} shifting from a quadratic to a linear dependence on the applied field E_y near $E_y=0$. The behavior being illustrated in Figs. 11(*a*) and 11(*b*) is akin to a linear d_{31} mode of piezoelectric behavior. However, note that for the film this behavior is a result of both the intrinsic piezoelectric response of the domains and an extrinsic response due to the motion of domain walls and the evolution of the domain structure.

As the film strain decreases the central *c*-domain seen in Fig. 9(*b*) moves toward the bottom electrode and a greater volume of the film is occupied by the *c*-domains that tend to increase the averaged film polarization. A second transition in the film behavior occurs at a strain of $\varepsilon_{xx}=0.38\varepsilon_0$ when the central *c*-domain intersects the bottom electrode, as shown in Fig. 9(*c*). This change in domain structure morphology also causes a mild transition in the piezoelectric response of the film as illustrated by the kink in the P_s versus ε_{xx} response shown in Fig. 10(*b*).

Figure 12 elucidates the two different types of nonlinear dielectric behavior in ferroelectric thin films; Fig. 12(*a*) is the paraelectric behavior and Fig. 12(*b*) is the ferroelectric behavior. As shown in Fig. 10(*b*), for zero applied electric field the film can be either nonpolar or polar depending on the level of film strain. In the nonpolar case Fig. 12(*a*) shows that for zero applied field, the electric displacement at point *A* is zero. The application of external field in the positive direction induces polarization in the film and consequently its domain structure evolves, as shown in Figs. 8(*a*)–8(*c*). At the critical field value the electric displacement reaches point *B* where the microstructure switches from the polydomain structure to a homogeneous, but stressed, *c*-domain following branch $B-B'$. An additional increase in the applied field corresponds to the $B'-C$ branch of Fig. 12(*a*), while a decrease in the external field causes the $B'-G$ branch. At point *G*, the material switches to a *c*-domain with opposite polarization following branch $G-T-G'$. Branches $C'-H$ and $H-T'-H'$ are symmetric with respect to the origin to $C-G$ and $G-T-G'$, respectively, while branches $A-F$ and $F-F'$ are symmetric to $A-B$ and $B-B'$ and correspond to negative applied field. Note that between

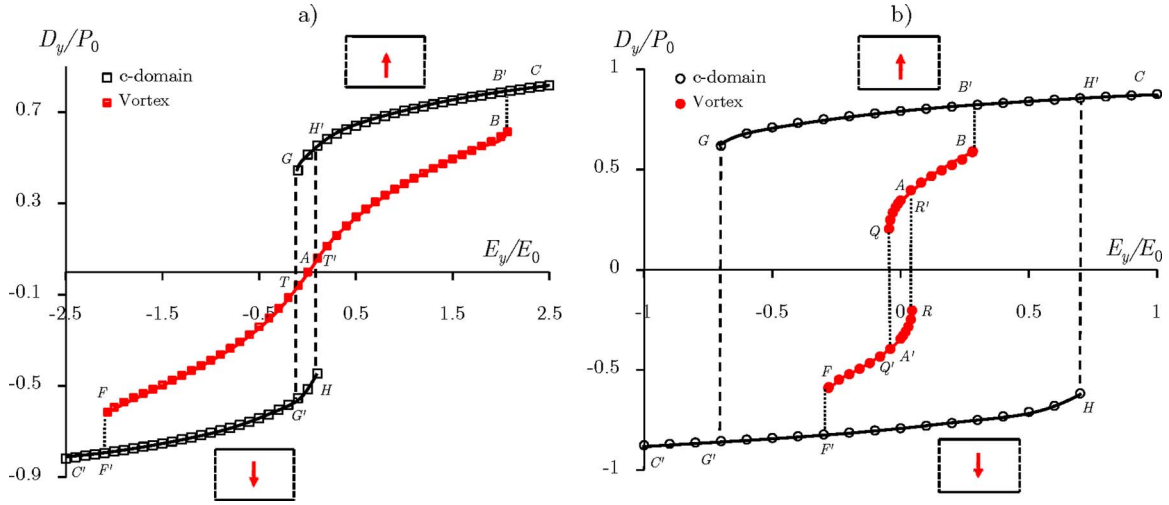

Fig. 12 Dielectric behavior of ferroelectric thin films as characterized by the numerical simulations presented in this article for domain periodicity equal to $18l_0$, film thickness equal to $10l_0$, and (*a*) film strain $\varepsilon_{xx}=\varepsilon_0$, which corresponds to a nonpolar domain structure for zero applied field and (*b*) film strain $\varepsilon_{xx}=0.4\varepsilon_0$ for which a polar structure was obtained for a zero field, as shown in Figs. 10(*a*) and 10(*b*).

points G and H, three distinct equilibrium domain configurations exist: two homogeneous c-domains with opposite polarization and a nonpolar polydomain vortex structure. If transitions between each of these states can be controlled, these results suggest the possibility of using film strain to allow for a tristate memory device.

Figure 12(b) illustrates the behavior of the ferroelectric domain structure. Such films have nonzero net polarization for zero applied field. The application of a positive electric field causes the nonlinear dielectric behavior shown in branches $A-B$ and $B-B'$, similar to the nonpolar case. If negative field is applied to the initial positive polar structure then the material reaches point Q at which point its microstructure switches following branch $Q-Q'$ to a corresponding vortex domain configuration with negative net polarization. In this case branches $A'-R$ and $R-R'$ are the corresponding dielectric behavior for positive applied field, indicating the reverse switching response between the polydomain domain structures. Notice that the switching to a homogeneous c-domain in the ferroelectric case shown in Fig. 12(b) occurs for critical field values that are significantly lower than the corresponding values in the nonpolar case in agreement with the results shown in Figs. 10(a) and 10(b). Figures 9(a) and 9(b) illustrate the fundamental role that film strain plays in the electromechanical properties of electroded ferroelectric thin films.

6 Concluding Remarks

The effects of film thickness and imposed electromechanical loading conditions on the domain morphology, its evolution, and the resultant properties of ferroelectric thin films has been investigate in this paper. Numerical results are computed using a finite element method, which is based on a phase-field model. The findings show that the film strain has a significant effect on the minimum energy equilibrium states. For insulated films with relatively low film strain, alternating c-domain patterns with closure domains near the surface constitute the energetically favorable domain structures in $BaTiO_3$ thin films. The domain periodicity for such minimum energy structures is found to depend on the film thickness for different values of film strain in accordance with the Kittel law. For electroded films, the effect of applied electric field on the domain morphology and evolution, and on the dielectric, piezoelectric, and electrostrictive behavior of the ferroelectric thin film is also examined in this paper. The results demonstrate that the film strain significantly affects the equilibrium domain structure and its evolution in ferroelectric thin films. Specifically, the calculations have uncovered a transition for paraelectric to ferroelectric film response that is controlled by the films strain. Large film strains favor paraelectric-like response and stabilize the polydomain structure to high levels of applied electric field, while smaller film strains allow for ferroelectric-like response with switching occurring between polar polydomain states.

Acknowledgment

We gratefully acknowledge the support for this work from the NSF through Grant No. CMMI-0719071 and from the ONR through Contract No. N00014-07-1-0469.

Appendix

Equation (12) presented the general form of the Helmholtz free energy used in this paper. For a coordinate system aligned with the [100] direction, the specific form used to fit the dielectric, piezoelectric, and elastic properties of ferroelectric single crystals that undergo a cubic to tetragonal phase transformation is taken by Su and Landis [1] and is given in Eq. (A1)

$$\begin{aligned}
\psi = {} & \frac{a_0}{2}(P_{1,1}^2 + P_{2,2}^2 + P_{3,3}^2 + P_{1,2}^2 + P_{2,1}^2 + P_{1,3}^2 + P_{3,1}^2 + P_{2,3}^2 \\
& + P_{3,2}^2) + \frac{a_1}{2}(P_1^2 + P_2^2 + P_3^2) + \frac{a_2}{4}(P_1^4 + P_2^4 + P_3^4) \\
& + \frac{a_3}{2}(P_1^2P_2^2 + P_2^2P_3^2 + P_1^2P_3^2) + \frac{a_4}{6}(P_1^6 + P_2^6 + P_3^6) \\
& + a_6(P_1^4(P_2^2 + P_3^2) + P_2^4(P_1^2 + P_3^2) + P_3^4(P_1^2 + P_2^2)) \\
& + \frac{a_5}{4}(P_1^4P_2^4 + P_2^4P_3^4 + P_1^4P_3^4) - \frac{b_1}{2}(\varepsilon_{11}P_1^2 + \varepsilon_{22}P_2^2 + \varepsilon_{33}P_3^2) \\
& - \frac{b_2}{2}((\varepsilon_{22} + \varepsilon_{33})P_1^2 + (\varepsilon_{11} + \varepsilon_{33})P_2^2 + (\varepsilon_{11} + \varepsilon_{22})P_3^2) \\
& - b_3((\varepsilon_{12} + \varepsilon_{21})P_1P_2 + (\varepsilon_{13} + \varepsilon_{31})P_1P_3 + (\varepsilon_{23} + \varepsilon_{32})P_2P_3) \\
& + \frac{c_1}{2}(\varepsilon_{11}^2 + \varepsilon_{22}^2 + \varepsilon_{33}^2) + c_2(\varepsilon_{11}\varepsilon_{22} + \varepsilon_{11}\varepsilon_{33} + \varepsilon_{22}\varepsilon_{33}) \\
& + \frac{c_3}{2}((\varepsilon_{12} + \varepsilon_{21})^2 + (\varepsilon_{13} + \varepsilon_{31})^2 + (\varepsilon_{23} + \varepsilon_{32})^2) \\
& + \left(\frac{f_1}{2}\varepsilon_{11}^2 + \frac{f_2}{2}(\varepsilon_{22}^2 + \varepsilon_{33}^2) + f_3(\varepsilon_{11}\varepsilon_{22} + \varepsilon_{11}\varepsilon_{33}) + f_4\varepsilon_{22}\varepsilon_{33}\right. \\
& \left. + \frac{f_5}{2}((\varepsilon_{12} + \varepsilon_{21})^2 + (\varepsilon_{13} + \varepsilon_{31})^2) + \frac{f_6}{2}(\varepsilon_{23} + \varepsilon_{32})^2\right)P_1^2 \\
& + \left(\frac{f_1}{2}\varepsilon_{22}^2 + \frac{f_2}{2}(\varepsilon_{11}^2 + \varepsilon_{33}^2) + f_3(\varepsilon_{11}\varepsilon_{22} + \varepsilon_{22}\varepsilon_{33}) + f_4\varepsilon_{11}\varepsilon_{33}\right. \\
& \left. + \frac{f_5}{2}((\varepsilon_{12} + \varepsilon_{21})^2 + (\varepsilon_{23} + \varepsilon_{32})^2) + \frac{f_6}{2}(\varepsilon_{13} + \varepsilon_{31})^2\right)P_2^2 \\
& + \left(\frac{f_1}{2}\varepsilon_{33}^2 + \frac{f_2}{2}(\varepsilon_{11}^2 + \varepsilon_{22}^2) + f_3(\varepsilon_{11}\varepsilon_{33} + \varepsilon_{22}\varepsilon_{33}) + f_4\varepsilon_{11}\varepsilon_{22}\right. \\
& \left. + \frac{f_5}{2}((\varepsilon_{13} + \varepsilon_{31})^2 + (\varepsilon_{23} + \varepsilon_{32})^2) + \frac{f_6}{2}(\varepsilon_{12} + \varepsilon_{21})^2\right)P_3^2 \\
& + \left(\frac{g_1}{4}\varepsilon_{11} + \frac{g_2}{4}(\varepsilon_{22} + \varepsilon_{33})\right)P_1^4 + \left(\frac{g_1}{4}\varepsilon_{22} + \frac{g_2}{4}(\varepsilon_{11} + \varepsilon_{33})\right)P_2^4 \\
& + \left(\frac{g_1}{4}\varepsilon_{33} + \frac{g_2}{4}(\varepsilon_{11} + \varepsilon_{22})\right)P_3^4 + \frac{g_3}{4}(\varepsilon_{12} + \varepsilon_{21})(P_1P_2^3 + P_2P_1^3) \\
& + \frac{g_3}{4}(\varepsilon_{13} + \varepsilon_{31})(P_1P_3^3 + P_3P_1^3) + \frac{g_3}{4}(\varepsilon_{23} + \varepsilon_{32})(P_2P_3^3 + P_3P_2^3) \\
& + \frac{1}{2\kappa_0}((D_1 - P_1)^2 + (D_2 - P_2)^2 + (D_3 - P_3)^2) \qquad \text{(A1)}
\end{aligned}$$

In the equation above $\kappa_0 = 8.854 \times 10^{-12}$ V m/C, and

$$a_1 = -0.668325E_0/P_0, \quad a_2 = -3.80653E_0/P_0^3,$$

$$a_3 = 0.78922E_0/P_0^3, \quad a_4 = 12.4421E_0/P_0^5$$

$$a_5 = 368E_0/P_0^7, \quad a_6 = 0.134226E_0/P_0^5$$

$$b_1 = 2.54138E_0/\varepsilon_0P_0, \quad b_2 = 1.74267E_0/\varepsilon_0P_0,$$

$$b_3 = 0.399353E_0/\varepsilon_0P_0$$

$$c_1 = 2.04999\sigma_0/\varepsilon_0, \quad c_2 = 0.971673\sigma_0/\varepsilon_0, \quad c_3 = 1.27976\sigma_0/\varepsilon_0$$

$$f_1 = 0.663581E_0/\varepsilon_0^2P_0, \quad f_2 = 0.841326E_0/\varepsilon_0^2P_0,$$

$$f_3 = -0.170635E_0/\varepsilon_0^2P_0$$

$$f_4 = 0.687281E_0/\varepsilon_0^2 P_0, \quad f_5 = 0.106647E_0/\varepsilon_0^2 P_0,$$

$$f_6 = 0.213294E_0/\varepsilon_0^2 P_0$$

$$g_1 = -3.66149E_0/\varepsilon_0 P_0^3, \quad g_2 = 6.27423E_0/\varepsilon_0 P_0^3,$$

$$g_3 = -1.21644E_0/\varepsilon_0 P_0^3$$

where $\sigma_0 = E_0 P_0/\varepsilon_0 = 692 \times 10^6$ N/m^2. In addition, $P_0 = 0.26$ C/m^2, $\varepsilon_0 = 0.0082$, and $E_0 = 2.182 \times 10^7$ V/m correspond to properties of monodomain single crystal barium titanate at room temperature.

The parameter a_0 appearing in Eq. (A1) determines the domain wall thickness. If $a_0 = 10^{-10}$ V m^3/C then $l_0 = 1$ nm, and therefore the 180 deg domain wall has thickness equal to 2 nm, which agrees with experimental observations [27].

References

[1] Su, Y., and Landis, C. M., 2007, "Continuum Thermodynamics of Ferroelectric Domain Evolution: Theory, Finite Element Implementation, and Application to Domain Wall Pinning," J. Mech. Phys. Solids, **55**, pp. 280–305.

[2] Kontsos, A., and Landis, C. M., 2009, "Computational Modeling of Domain Wall Interactions With Dislocations in Ferroelectric Crystals," Int. J. Solids Struct., **46**, pp. 1491–1498.

[3] Cao, W., and Cross, W., 1991, "Theory of Tetragonal Twin Structures in Ferroelectric Perovskites With a First-Order Phase Transition," Phys. Rev. B, **44**(1), pp. 5–12.

[4] Duan, W., and Liu, Z.-R., 2006, "Theoretical Modeling and Simulations of Perovskite Ferroelectrics: From Phenomenological Approaches to Ab Initio," Curr. Opin. Solid State Mater. Sci., **10**, pp. 40–51.

[5] Scott, J. F., and Dawber, M., 2000, "Oxygen-Vacancy Ordering as a Fatigue Mechanism in Perovskite Ferroelectrics," Appl. Phys. Lett., **76**(25), pp. 3801–3803.

[6] Scott, J. F., 2007, "Applications of Modern Ferroelectrics," Science, **315**, pp. 954–959.

[7] Landau, L. A. L. E., 1935, "On the Theory of the Dispersion of Magnetic Permeability in Ferromagnetic Bodies," Phys. Z. Sowjetunion, **8**(153), pp. 101–108.

[8] Kittel, C., 1946, "Theory of the Structure of Ferromagnetic Domains in Films and Small Particles," Phys. Rev., **70**(11-12), pp. 965–971.

[9] Mitsui, T., and Furuichi, J., 1953, "Domain Structure of Rochelle Salt and KH_2PO_4," Phys. Rev., **90**(2), pp. 193–202.

[10] Catalan, G., Scott, J. F., Schilling, A., and Gregg, J. M., 2007, "Wall Thickness Dependence of the Scaling Law for Ferroic Stripe Domains," J. Phys.: Condens. Matter, **19**, p. 022201.

[11] Streiffer, S. K., Eastman, J. A., Fong, D. D., Thompson, C., Munkholm, A., Ramana Murty, M. V., Auciello, O., Bai, G. R., and Stephenson, G. B., 2002, "Observation of Nanoscale 180° Stripe Domains in Ferroelectric $PbTiO_3$ Thin Films," Phys. Rev. Lett., **89**(6), p. 067601.

[12] Takahashi, R., Dahl, O., Eberg, E., Grepstad, J. K., and Tybell, T., 2008, "Ferroelectric Stripe Domains in $PbTiO_3$ Thin Films: Depolarization Field and Domain Randomness," J. Appl. Phys., **104**, p. 064109.

[13] Thompson, C., Fong, D. D., Wang, R. V., Jiang, F., Streiffer, S. K., Latifi, K., Eastman, J. A., Fuoss, P. H., and Stephenson, G. B., 2008, "Imaging and Alignment of Nanoscale 180° Stripe Domains in Ferroelectric Thin Films," Appl. Phys. Lett., **93**, p. 182901.

[14] Schilling, A., Adams, T. B., Bowman, R. M., Gregg, J. M., Catalan, G., and Scott, J. F., 2006, "Scaling of Domain Periodicity With Thickness Measured in $BaTiO_3$ Single Crystal Lamellae and Comparison With Other Ferroics," Phys. Rev. B, **74**, p. 024115.

[15] Fu, H., and Bellaiche, L., 2003, "Ferroelectricity in Barium Titanate Quantum Dots and Wires," Phys. Rev. Lett., **91**(25), p. 257601.

[16] Wu, Z., Huang, N., Liu, Z., Wu, J., Wenhui, D., and Gu, B.-L., 2004, "Ferroelectricity in $Pb(Zr_{0.5}Ti_{0.5})O_3$ Thin Films: Critical Thickness and 180° Stripe Domains," Phys. Rev. B, **70**, p. 104108.

[17] Lai, B.-K., Ponomareva, I., Naumov, I. I., Kornev, I., Fu, H., Bellaiche, L., and Salamo, G. J., 2006, "Electric-Field Induced Domain Evolution in Ferroelectric Ultrathin Films," Phys. Rev. Lett., **96**, p. 137602.

[18] Lai, B.-K., Ponomareva, I., Kornev, I., Bellaiche, L., and Salamo, G. J., 2007, "Domain Evolution of $BaTiO_3$ Ultrathin Films Under an Electric Field: A First-Principles Study," Phys. Rev. B, **75**, p. 085412.

[19] Lai, B.-K., Ponomareva, I., Kornev, I., Bellaiche, L., and Salamo, G. J., 2007, "Thickness Dependency of 180 Stripe Domains in Ferroelectric Ultrathin Films: A First-Principles-Based Study," Appl. Phys. Lett., **91**, p. 152909.

[20] Chen, L. Q., 2002, "Phase-Field Modeling for Microstructure Evolution," Annu. Rev. Mater. Res., **32**, pp. 113–140.

[21] Brennan, C., 1995, "Landau Theory of Thin Ferroelectric Films," Integr. Ferroelectr., **9**, pp. 335–346.

[22] Li, Y. L., Hu, S. Y., Liu, Z. K., and Chen, L. Q., 2001, "Phase-Field Model of Domain Structures in Ferroelectric Thin Films," Appl. Phys. Lett., **78**(24), pp. 3878–3880.

[23] Schrade, D., Mueller, R., Xu, B. X., and Cross, D., 2007, "Domain Evolution in Ferroelectric Materials: A Continuum Phase Field Model and Finite Element Implementation," Comput. Methods Appl. Mech. Eng., **196**, pp. 4365–4374.

[24] Dayal, K., and Bhattacharya, K., 2007, "A Real Space Non-Local Phase-Field Model of Ferroelectric Domain Patterns in Complex Geometries," Acta Mater., **55**, pp. 1907–1917.

[25] Li, W., and Landis, C. M., 2008, "Phase-Field Modeling of Domain Switching Near Crack Tips in Single Crystal Ferroelectrics," Proc. SPIE, **6929**, p. J9290.

[26] Gurtin, M. E., 1996, "Generalized Ginzburg-Landau and Cahn-Hilliard Equations Based on a Microforce Balance," Physica D, **92**, pp. 178–192.

[27] Scott, J. F., 2006, "Nanoferroelectrics: Statics and Dynamics," J. Phys.: Condens. Matter, **18**, pp. R361–R386.